Enhanced pore space analysis by use of μ-CT, MIP, NMR, and SIP

Zeyu Zhang [1], Sabine Kruschwitz [2, 3], Andreas Weller [4], Matthias Halisch [5]

[1] Southwest Petroleum University, School of Geoscience and Technology, 610500 Chengdu, China

[2] Federal Institute for Material Research and Testing (BAM), D-12205 Berlin, Germany

[3] Technische Universität Berlin, Institute of Civil Engineering, D-13355 Berlin, Germany

[4] Clausthal University of Technology, Institute of Geophysics, D-38678 Clausthal-Zellerfeld, Germany

[5] Leibniz Institute for Applied Geophysics (LIAG), D-30655 Hannover, Germany

Correspondence to: Zeyu Zhang (zeyuzhangchina@163.com)

Abstract

We investigate the pore space of rock samples with respect to different petrophysical parameters using various methods, which provide data upon pore size distributions, including micro computed tomography (μ-CT), mercury intrusion porosimetry (MIP), nuclear magnetic resonance (NMR), and spectral induced polarization (SIP). The resulting cumulative distributions of pore volume as a function of pore size are compared. Considering that the methods differ with regard to their limits of resolution, a multiple length scale characterization of the pore space is proposed, that is based on a combination of the results from all of these methods. The approach is demonstrated using samples of Bentheimer and Röttbacher sandstone. Additionally, we compare the potential of SIP to provide a pore size distribution with other commonly used methods (MIP, NMR). The limits of resolution of SIP depend on the usable frequency range (between 0.002 Hz and 100 Hz). The methods with similar resolution show a similar behavior of the cumulative pore volume distribution in the overlapping pore size range. We assume that μ-CT and NMR provide the pore body size while MIP and SIP characterize the pore throat size. Our study shows that a good agreement between the pore radii distributions can only be achieved if the curves are adjusted considering the resolution and pore volume in the relevant range of pore radii. The MIP curve with the widest range in resolution should be used as reference.

Keywords: Pore Space Analysis, Joint Interpretation, Fractal Dimension, Spectral Induced Polarization

1 Introduction

Transport and storage properties of reservoir rocks are determined by the size and arrangement of the pores. In this paper we use the term geometry to refer to the relevant pore sizes, such as the pore throat radius, pore body radius, body to throat ratio, shape of the pore, and pore volume corresponding to certain pore radius. Different methods have been developed to determine the pore size distribution of rocks. These methods are based on different physical principles. Therefore, it can be expected that the methods recognize different geometries and sizes. Additionally, the ranges of pore sizes that are resolved by the methods are different (Meyer et al., 1997). Rouquerol et al. (1994) stated in the conclusions of their recommendations for the characterization of porous solids that no experimental method provides the absolute value of parameters such as porosity, pore size, surface area, and surface roughness. It should be noted that these parameters indicate a fractal nature. That means that the value of the parameter depends on the spatial resolution of the method.

An enhanced pore space analysis using different methods should be able to provide a better description of the pore space over a wide range of pore sizes. Our study of pore space analysis is based on the following methods: micro computed tomography (μ-CT), mercury intrusion porosimetry (MIP), nuclear magnetic

resonance (NMR), and spectral induced polarization (SIP). The first three methods can be regarded as standard methods to derive a pore size distribution. Since these methods can reveal the inner structure of the rocks, they are widely applied in geosciences (e.g. Halisch et al., 2016b, Mees et al., 2003, Behroozmand et al., 2015, Weller et al., 2015). The main aim of our paper is to integrate an electrical method in this study. Electrical conductivity and polarizability (or real and imaginary part of electrical conductivity) are fundamental physical properties of porous materials. The SIP method measures the low-frequency electric behavior of rocks and soil material that can be efficiently represented by a complex electric conductivity (e.g. Slater and Lesmes, 2002). The electric properties of a porous material depend to a large extent on key parameters including the porosity, the grain and pore size distribution, the specific internal surface, the tortuosity, the saturation and the chemical composition of the pore-filling fluids. SIP is a non-destructive method that can be applied to characterize the geometry of the pore system. Müller-Huber et al. (2018) proposed the integration of SIP in a combined interpretation with NMR and MIP measurements for carbonate rocks in order to use the partly complementary information of each method. The SIP method is used to explore correlations between parameters derived from complex conductivity spectra and specific pore space properties. We go a step ahead and compare directly the pore size distributions derived from the different methods. Procedures to derive pore size distributions from induced polarization (IP) data have been proposed only recently (Florsch et al., 2014; Revil et al., 2014; Niu and Zhang 2017; Zhang et al., 2017).

We are aware that further methods can be applied for the characterization of pore size distribution, e.g. synchrotron-radiation-based computed tomography (Peth et al., 2008), focused ion beam tomography (Keller et al., 2011), transmission electron microscopy (Gaboreau et al., 2012), scanning electron microscopy (SEM), ^{14}C labeled methylmethacrylate method (Kelokaski et al., 2005), and gas adsorption and desorption method (BET) (Avnir and Jaroniec, 1989).

Our study presents an approach to describe and quantify the pore space of porous material by combining the results of methods with different resolution. Samples of Bentheimer and Röttbacher sandstone are investigated by µ-CT, MIP, NMR, and SIP. Each method provides the pore size distribution in a limited range of resolution. It is not our intention to combine the data of the different methods in a joint inversion to get a more reliable pore size distribution as proposed by Niu and Zhang (2017). We prefer to compare the resulting pore size distributions to each other to get two different pore radii distributions, one for the pore body radius and one for the pore throat radius. The comparison of the two curves enables the determination of the ratio between pore body and pore throat radius. A joint inversion that ignores the difference between pore body and pore throat provides a simplified model that ignores the complexity of pore space geometry.

Considering the fractal nature of pore space geometry an attempt is made to determine the fractal dimension of the pore volume distribution for the two investigated samples. The fractal dimension is a

81 useful parameter for up-and downscaling of geometrical quantities. Zhang and Weller (2014) investigated

82 the fractal behavior of the pore volume distribution by capillary pressure curves and NMR T_2 distributions

83 of sandstones. Considering the differences in fractal dimension resulting from the two methods, they

84 concluded a differentiation into surface dimension and volume dimension. Additionally, the fractal

85 dimension is used in methods of permeability prediction (e.g. Pape et al., 2009).

86 **2 Theory**

87 The pore size distribution resulting from different methods has to be compared and evaluated. We prefer a

88 comparison based on the cumulative volume fraction of pores V_c, which is expressed by

89
$$V_c = \frac{V(<r)}{V_p} , \tag{1}$$

90 with V_p being the total pore volume, and $V(<r)$ the cumulative volume of pores with radii less than r. A

91 graph displaying the logarithm of V_c versus the logarithm of the pore radius offers the advantage that the

92 slope of the curves is related to the fractal dimension of the pore volume (Zhang and Weller, 2014).

93 Fractal theory is applied to describe the structure of geometric objects (Mandelbrot, 1977, 1983). At

94 molecular size and microscopic range, surfaces of most materials including those of natural rocks show

95 irregularities and defects that appear to be self-similar upon variation of resolution (Avnir et. al, 1984). A

96 self-similar object is characterized by similar structures at different scales. The regularity of self-similar

97 structures can be quantified by the parameter of fractal dimension D. Pape et al. (1982) first proposed a

98 fractal model (the so called 'pigeon-hole model' or 'Clausthal Concept') for the geometry of rock pores.

99 Fractal dimension describes the size of geometric objects as a function of resolution. This parameter has

100 proved to be useful in the comparison of different methods that determine distributions of pores in

101 sandstones and carbonates (e.g. Zhang and Weller, 2014, Ding et al., 2017).

102 From MIP, the entry sizes of pores and cavities, which is referred to as pore throat radius r_t, can be

103 determined according to the Washburn-equation (Washburn, 1921)

104
$$r_t = -\frac{2 \cdot \gamma \cdot \cos\theta}{P_c} , \tag{2}$$

105 with $\gamma = 0.48$ N/m being the surface tension of mercury, $\theta = 140°$ the contact angle between mercury and

106 the solid minerals, and P_c the pressure of the liquid mercury that is referred to as capillary pressure.

107 Starting with low pressure, the pores with larger pore throats are filled with mercury. While increasing the

108 pressure, the pores with smaller throats are filled. Reaching a certain pressure level P_c, a cumulative

109 volume of mercury (V_{Hg}) has intruded into the sample that corresponds to the pore volume being accessible

110 by pore throat radii larger or equal r_t according to Eq. (2). Figure 1 shows a 2D image of the pore space of

111 sample BH5-2 (information is given in Section 3) indicating the pore throat radius r_t as measured by MIP

112   by red arrows. Fluid flow properties, and hence the injection pressure of mercury, solely depends upon the
113   narrowest pore diameter in the flow path that corresponds to the pore throat diameter. The cumulative
114   volume of mercury V_{Hg} corresponds to the pore volume $V(>r_t)$. It should be noted that the volume of larger
115   pores, which are shielded by narrower throats, is attributed to the pore throat radius (e.g. Kruschwitz et al.,
116   2016). Knowing the total pore volume V_p, the saturation of the sample with mercury S_{Hg} can be determined.
117   A conventional capillary pressure curve displays the relationship between the saturation of the sample with
118   mercury S_{Hg} as a function of capillary pressure P_c (e.g. Thomeer, 1960). Using the following simple
119   transformations

120
$$S_{Hg} = \frac{V_{Hg}}{V_p} = \frac{V(>r_t)}{V_p} = \frac{V_p - V(<r_t)}{V_p} = 1 - V_c , \qquad (3)$$

121   the cumulative volume fraction of pores V_c as defined in Eq. (1) can be determined as a function of r_t.
122   The NMR relaxometry experiment records the decay of transversal magnetization. The measured
123   transversal decay curve is decomposed in a distribution of relaxation times $b(T_2)$. The individual relaxation
124   time T_2 is attributed to a pore space with a certain surface to volume ratio A/V by

125
$$\frac{1}{T_2} = \rho\left(\frac{A}{V}\right), \qquad (4)$$

126   with ρ being the surface relaxivity. Considering that for a capillary tube model with cylindrical pores of
127   radius r, the surface to volume ratio equals $2/r$, we get the following linear relationship between pore radius
128   r and relaxation time T_2 (e.g. Kleinberg, 1996):

129
$$r = 2\rho T_2 . \qquad (5)$$

130   It should be noted that the NMR method resolves the radius r_b that corresponds to the maximal distance to
131   the pore wall. It can be represented by the pore radius of the largest sphere that can be placed inside this
132   pore as shown in Figure 1.
133   Another approach to derive a pore size distribution is based on the SIP method. Relations between grain or
134   pore size and IP parameters have been reported in a variety of studies (e.g. Slater and Lesmes, 2002; Scott
135   and Barker, 2003; Binley et al., 2005; Leroy et al., 2008; Revil and Florsch, 2010). Polarization effects of
136   natural material are caused by different charging and discharging processes of some polarizing elements
137   such as grain surface, pore throat, membrane, and electrical double layer. Following an approach proposed
138   by Schwarz (1992), the complex conductivity of an individual polarization element can be presented by a
139   Debye model. It is assumed that the recorded spectra result from a superposition of polarization processes
140   characterized by different relaxation times. This approach has been adopted to generate synthetic spectra of
141   electrical conductivity from distributions of grain sizes (e.g. Revil and Florsch, 2010) or pore sizes (e.g.
142   Niu and Zhang, 2017).

143 A decomposition of the spectra is needed to derive the relaxation time distribution. Florsch et al. (2014)
144 demonstrated that a variety of models can be used as kernel for the decomposition of the spectra. Revil et al.
145 (2014) compare the results of Debye and Warburg decomposition. Their argumentation, which is based on
146 mechanistic grain size models describing the polarization of charged colloidal particles and granular
147 material, supports the application of the Warburg decomposition that results in a narrower distribution of
148 polarization length scales. It should be noted that a uniform grain size does not automatically generate a
149 uniform pore size. Besides it can be clearly seen by the scanning electrode microscopy images that the
150 investigated sandstones feature a distinct range of both, grain and pore (throat) sizes. Considering that the
151 pore size and not the grain size controls the polarization of sandstones, as observed by different authors (e.g.
152 Scott and Barker, 2003; Niu and Revil, 2016), a wider distribution of length scales can be expected.
153 According to our opinion, there are no clear indications for superiority of the Warburg decomposition. Up
154 to now, a theoretical model that confirms the validity of the Warburg model in describing the polarization
155 of a simple pore space geometry has not been presented. Therefore, we prefer to use the Debye
156 decomposition, which has proved to be a useful tool in the processing of IP data in both time and frequency
157 domain (e.g. Terasov and Titov, 2007; Weigand and Kemna, 2016). The algorithm described by Nordsiek
158 and Weller (2008) provides the electrical relaxation time distribution as well as the total chargeability from
159 complex conductivity spectra.

160 According to the assumption that the electrical relaxation time and pore size are related to each other, the
161 specific chargeability at a certain relaxation time corresponds to the pore volume attributed to a certain pore
162 size, and the total chargeability is attributed to the total pore volume of the sample. The volume fraction V_c
163 corresponds to the ratio of cumulative chargeability to total chargeability. To transform the relaxation time
164 distribution into a pore size distribution, we adopt the approach proposed by Schwarz (1962) and applied
165 by Revil et al. (2012) for the Stern layer polarization model:

166
$$r = \sqrt{2\tau D_{(+)}} \; , \tag{6}$$

167 with $D_{(+)}$ being the diffusion coefficient of the counter-ions in the Stern layer and τ being the relaxation
168 time. Originally, this equation describes the relation between the radius of spherical particles in an
169 electrolyte solution and the resulting relaxation time. Though it remains arguable whether the radius of
170 spherical grains can be simply replaced by the pore radius (Weller et al., 2016), we generally follow this
171 approach. Additionally, we assume a constant diffusion coefficient $D_{(+)} = 3.8 \times 10^{-12}$ m²/s as proposed by
172 Revil (2013).

173 The signal amplitude at a given relaxation time corresponds to the pore volume related to the pore radius
174 determined by Eq. (6). Considering the experience that the polarization is related to the specific surface
175 area per unit pore volume (e.g. Weller et al., 2010), we assume that the IP signals are caused by the ion-
176 selected active zones in the narrow pores that are comparable with the pore throats. Their size is quantified
177 by the pore throat radius r_t. Following the procedure proposed by Zhang et al. (2017), the cumulative

178 volume fraction V_c corresponds to the ratio of cumulative chargeability to total chargeability. Considering
179 the restricted range of pore radii (0.1-25 μm) resolved by SIP, a correction of the maximum V_c becomes
180 necessary.

181 **3 Samples and methods**

182 For this study, two different sandstone samples have been used: first, a Bentheimer sandstone, sample
183 BH5-2. The shallow-marine Bentheimer sandstone was deposited during the Early Cretaceous (roughly 140
184 million years ago) and forms an important reservoir rock for petroleum (Dubelaar et al., 2015). This
185 sandstone is widely used for systematic core analysis due its simple mineralogy and the quite homogeneous
186 and well-connected pore space. It is composed out of 92% quartz, contains some feldspar and about 2.5
187 vol.-% of kaolinite (Peksa et al., 2015), which is a direct alteration product of the potassium-bearing
188 feldspar minerals. Accordingly, surface area as well as surface relaxivity values are mostly controlled by
189 the kaolinite for this rock.
190 Secondly, a Röttbacher sandstone, sample RÖ10B, has been used. The Röttbacher sandstone is a fine-
191 grained, more muscovite-illite containing, and rather homogeneous material that was deposited during the
192 Lower Triassic era (roughly 250 million years ago). It is suitable for solid stonework and has been widely
193 used as building material for facades as well as for indoor and outdoor flooring. The Röttbacher sandstone
194 was included in a study on the relationship of pore throat sizes and SIP relaxation times reported by
195 Kruschwitz et al. (2016). This sandstone consists mostly of quartz, but features a higher amount of clay
196 minerals than the Bentheimer sample. Additionally, Fe-bearing minerals (e.g. haematite) have been formed
197 during its arid depositional environment, giving this sandstone a distinct reddish color. Accordingly,
198 surface area as well as surface relaxivity are dominated by the clay and Fe-bearing minerals and should be
199 significantly different than for the BH5-2 sample.
200 The experimental methods used in this study include digital image analysis (DIA) based upon micro
201 computed tomography (μ-CT), mercury intrusion porosimetry (MIP), nuclear magnetic resonance (NMR),
202 and spectral induced polarization (SIP).
203
204 For this study, a nanotom S 180 X-ray μ-CT equipment (GE sensing and inspection technologies) has been
205 used. The sample size for μ-CT scanning is 2mm diameter and 4 mm length. For pore network separation, a
206 combination of manual thresholding and watershed algorithms has been applied to achieve the qualitatively
207 best separated pore space. Additionally, separation results have been cross checked with the images of
208 scanning electrode microscopy (SEM). More details on the DIA workflow can be found in Halisch et al.
209 (2016). The DIA of the 3-D μ-CT data sets provide for each individual pore the volume and the pore radius
210 of the largest sphere that can be placed inside this pore (maximum inscribed sphere method, e.g. Silin and
211 Patzek, 2006) as indicated by the blue circles in Figure 1. Note that Figure 1 displays a 2-D slice with

212   circles. The DIA is performed in 3-D volumes and provides spheres. The resulting equivalent pore radius is
213   referred to as pore body radius r_b. Though the true extent of the pore is not caught properly, the derived r_b
214   from DIA is a good estimate of the average radius. Adding up the pore volumes starting with the lowest
215   pore radius yields the cumulative volume fraction of pores V_c (Eq. (1)) as a function of the pore body radius
216   r_b. The µ-CT method can only resolve the part of the pore space with pore sizes larger than the spatial
217   resolution of the 3D image. Considering a voxel size of 1.75 µm of the 3D data set, and a minimum
218   extension of pores of two voxels in one direction, which can be separated by the algorithm, a minimum
219   pore size of 3.5 µm (or minimum pore radius of 1.75 µm) has to be regarded, as for this study, the CT
220   resolution limit is 1.75 µm. Therefore, the pore volume determined by µ-CT does not take into account the
221   pore space with radii smaller than 1.75 µm.

223   The MIP experiments have been conducted with the PASCAL 140/440 instrument from Thermo Fisher
224   (Mancuso et al., 2012), which covers a pressure range between 0.015 MPa and 400 MPa corresponding to a
225   pore throat radius range from (at best) 1.8 nm to 55 µm. The samples have been evacuated before the MIP
226   experiment.

228   The NMR experiments have been performed with a Magritek Rock Core Analyzer equipment operating at a
229   Larmor frequency of 2 MHz at room temperature (~ 20°C) and ambient pressure. After drying at 105°C for
230   more than 24 hours in vacuum, the samples have been fully saturated with tap water with a conductivity of
231   about 25 mS/m. NMR measurements can be calibrated to get the porosity of the sample. The early time
232   decay signal corresponds to the total water content. The range of resolved pore body radii depends on the
233   used value of surface relaxivity. The amplitude b attributed to an individual relaxation time T_2 is related to
234   the volume fraction of pores with the respective pore radius. Considering the larger pores, the resulting
235   radius corresponds to r_b. The smaller pore throats with lower volume yield a lower signal at shorter
236   relaxation times. The cumulative volume fraction of pores V_c is determined by adding up the individual b
237   values starting from the smallest relaxation time and normalizing to the total sum of all b values.

239   Complex conductivity spectra were recorded using a four-electrode sample holder as described by Schleifer
240   et al. (2002). The spectra were acquired with the impedance spectrometer ZEL-SIP04 (Zimmerman et al.,
241   2008) in a frequency range between 0.002 Hz and 45 kHz at a constant temperature of about 20 °C.
242   Considering that the complex conductivity spectra are affected by electromagnetic coupling effects,
243   Maxwell Wagner relaxation and dielectric effects at higher frequencies and by a lower signal to noise ratio
244   for lower frequencies, we focus on the frequency range between 0.01 Hz and 100 Hz. The samples were
245   fully saturated with a sodium-chloride solution with a conductivity of 100 mS/m. At least two
246   measurements were performed for each sample to verify the repeatability. Considering the limited

247 frequency interval, the SIP method solely resolves a range of pore radii that depends on the diffusion

248 coefficient. Hence, using $D_{(+)} = 3.8 \times 10^{-12}$ m²/s in Eq. (6), we get a range of pore radii between 0.1 μm and

249 10 μm. Smaller pore sizes are hidden by Maxwell Wagner relaxation and dielectric effects that are not

250 easily related to pore geometry.

251

252 Permeability measurements have been performed by using a steady-state gas permeameter (manufactured

253 by Westphal Mechanik, Celle, Germany), using nitrogen as the flowing fluid. This device features a so

254 called "Fancher-type" core holder as described by Rieckmann (1970). With this special type of core holder,

255 significantly lower confining pressures are needed than by using a conventional "Hassler-type" core holder

256 (12 bar for the "Fancher-type" core holder versus min. 35 - 50 bar for the "Hassler-type" core holder),

257 leading to much less initial mechanical influence (compaction) upon the sample material. Measurements

258 have been derived under steady-state flow conditions with accordingly low flow rates in range from 3 to 5

259 ml/min, leading to measured pressure differentials in range from 2 to 7 mbar from sample inlet to outlet.

260 The derived apparent permeability values have been corrected, to address the Klinkenberg-effect of gas

261 slippage (Klinkenberg, 1941; API, 1998). Due to the usage of a steady-state technique with low gas flow

262 rates, we consider that correction of the Forchheimer effect of inertial resistance can be neglected (API,

263 1998).

264 **4 Results**

265 **4.1 Petrophysical properties**

266 Figure 2 (A and C) gives 2-D impressions of the pore system of the Bentheimer sandstone sample. The

267 pore space in general is very well connected, featuring many large and open pores (Fig.2, A & C, blue

268 arrows) and can be described as a classical pore body – pore throat – pore body system. Small pores are

269 mostly found within the clayey agglomerations, which act as (macro) pore filling material (Fig. 2, A & C,

270 red arrows) and which are homogeneously distributed throughout the sample material. Figure 2 E gives an

271 impression of the 3-D pore distribution of this sandstone, derived by μ-CT image processing. This

272 favorable structure is directly reflected by the petrophysical properties of this sandstone. The sample

273 investigated in our study is characterized by a porosity of 0.238 measured by MIP, a gas-permeability of

274 4.25×10^{-13} m² determined by steady state permeameter (manufactured by Westphal Präzisionstechnik) with

275 a Fancher type core holder using nitrogen as the flowing fluid, and a specific surface area of 0.3 m²/g

276 determined by nitrogen adsorption method.

277 Figure 2 (B and D) shows the pore space of the Röttbacher sandstone sample from 2-D imaging techniques.

278 Though the (large) pore space is similar structured as it is for the Bentheimer (pore body-throat-body

279 system, Fig. 2, B & D, blue arrows), it is generally reduced (cemented) by clay minerals and features a

280 significantly higher amount of small pores within (Fig. 2, B & D, red arrows). Accordingly, pore space
281 related petrophysical properties classify a more compact rock, which is supported by the 3-D pore
282 distribution, derived by μ-CT image processing (Fig. 2, F). The sample used for this study features a
283 porosity of 0.166 measured by MIP, which is lower than for the Bentheimer sandstone. The gas-
284 permeability is 3.45×10^{-14} m², which is less than 10 % of the value determined for the Bentheimer
285 sandstone. The specific surface area has been measured with 1.98 m²/g and is hence nearly seven times
286 larger than for sample BH5-2, clearly underlining the impact of the clay content. The petrophysical
287 parameters for both samples are compiled in Table 1, whereas results from X-ray fluorescence analysis are
288 summarized in Table 2, regarding the most important chemical components of both sandstones that have
289 been used for this study.

290 **4.2 Pore volume fraction**

291 We applied the methods μ-CT, MIP, NMR, and SIP to get insight into the pore radius distribution of the
292 Bentheimer sandstone sample BH5-2. Figure 3 displays the resolved porosity ϕ_r as a function of pore radius
293 for μ-CT and MIP data. The cumulative pore volume while progressing from larger to smaller pores $V(>r)$
294 is normalized to the total volume of the sample V_s and results in the resolved porosity

295
$$\phi_r = \frac{V(>r)}{V_s} , \qquad (7)$$

296 which reaches the true porosity ϕ as threshold value for r approaching zero.
297 As shown in Figure 3, the μ-CT method identifies the largest pores with pore body radii of about 100 μm.
298 The resolved porosity ϕ_r reaches a value of 0.184 at the limit of resolution of the μ-CT method (r_b=1.75
299 μm). The nearly horizontal curve progression for $r < 17$ μm indicates that effectively no significant volume
300 of pores with radii lower than 17 μm was detected or quantified by μ-CT and DIA, respectively.
301 Accordingly, only μ-CT data for r > 17 μm will be taken into account for further analysis.
302 The MIP identifies the largest pore throats with a radius of about 30 μm. Reaching the limit of resolution of
303 the MIP, the resolved porosity approaches asymptotically the threshold value of 0.238. Though both
304 methods μ-CT and MIP yield the pore radius without any adjustable scaling factor, we observe differences
305 between the two curves $\phi_r(r)$ in Figure 3.
306 The Röttbacher sample was scanned with resolution 1.5 μm by μ-CT. As shown in Figure 4, the μ-CT
307 method identifies the largest pores with pore body radii of about 90 μm. The resolved porosity ϕ_r reaches a
308 value of 0.106 at the limit of resolution of the μ-CT method (r_b=1.5 μm). As observed for the Bentheimer
309 sandstone, the nearly horizontal curve progression for $r < 10$ μm indicates that no significant volume of
310 pores with radii lower than 10 μm were detected or quantified by μ-CT and DIA, respectively. Accordingly,
311 only μ-CT data for r > 10 μm will be taken into account for further analysis.

4.3 Pore radius distribution

The description and quantification of the pore space in three dimensions requires morphological parameters such as length, width, and thickness of individual pore segments. The parameters are extracted by image analysis software from 3-D µ-CT data. We determined the pore length (maximum length of Feret distribution), pore width (minimum width of Feret distribution), and the equivalent diameter of the analyzed pore segment that corresponds to the spherical diameter with equal voxel volume (Schmitt et al., 2016). The minima, maxima, and mean values of the geometrical parameters derived from µ-CT data of the two samples are compiled in Table 3.

The procedures described above result in an individual curve displaying the logarithm of V_c versus the logarithm of the pore radius for each method.

For Bentheimer sandstone, applying the transformation in Eq. (3) for the MIP data and assuming a true porosity of 0.238, the cumulative volume fraction of pores V_c can be displayed as a function of pore throat radius as shown in Figure 5. The MIP curve gets a fixed position in the plot of Figure 5 without the need for any scaling. It covers a wide range of pore throat radii between 0.0018 and 44.7 µm.

The curves resulting from other methods have to be adjusted considering the limits of the range of pore radii. The maximum of the µ-CT curve corresponds to $V_c = 1$ because no larger pore size has been detected by other methods. The maximum resolved porosity of the sample as detected by MIP reaches 0.238. The porosity determined by µ-CT reaches only 0.184 (Figure 3). This value corresponds to a fraction of 0.773 of the porosity determined by MIP. Therefore, the minimum of the µ-CT curve at the pore radius of 17 µm has to be adjusted at $V_c = 1 - 0.773 = 0.227$, because this fraction of pore volume is related to pore body radii smaller than 17 µm. The shift of the µ-CT curve to larger pore body radii in comparison with MIP is observed in this plot, too.

The T_2 relaxation time distribution of sample BH5-2 is plotted in Figure 6. It indicates a distinct maximum at a relaxation time of 330 ms and two weaker maxima at lower relaxation times. The T_2 relaxation time distribution is transformed into a curve showing the cumulative intensity as a function of T_2. The total intensity is attributed to the total pore volume. The volume fraction V_c corresponds to the ratio of cumulative intensity to total intensity. In order to get the curve V_c as a function of pore radius, the relaxation time T_2 has to be transformed into a pore radius using the surface relaxivity ρ as scaling factor in Eq. (5). Since both µ-CT and NMR method are sensitive to the pore body radius, we expect a similar V_c - r - curve in the overlapping range of pore body radii. Assuming a coincidence of the two curves at $V_c = 0.5$, the surface relaxivity is adjusted at $\rho = 54$ µm/s.

The complex conductivity spectra of the Bentheimer sample are displayed in Figure 7. Considering the frequency range between 0.01 and 100 Hz and $D_{(+)} = 3.8 \times 10^{-12}$ m²/s, the relaxation time distribution derived from SIP is attributed to a restricted range of pore radii between 0.1 µm and 10 µm. Assuming that the polarization signals originate from the pore throats, a similarity of pores size distributions resulting

347 from MIP and SIP can be expected. It should be noted that MIP provides the distribution for a wider range

348 of pore throat radii. Therefore, we adjust the value of V_c at the maximum radius of the SIP to the

349 corresponding value for the MIP curve.

350 As shown in Figure 4 for Röttbacher sandstone, the MIP identifies the largest pore throats with a radius of

351 about 50 µm. Reaching the limit of resolution of MIP, the resolved porosity gets the value of 0.166.

352 Applying the transformation in Eq. (3) on the MIP data and assuming a true porosity of 0.166, the

353 cumulative volume fraction of pores V_c is displayed as a function of pore radius as shown in Figure 8.

354 We suppose that the MIP method detects the whole pore volume, a porosity of 0.106 recognized by µ-CT

355 corresponds to 63.9% of the total pore volume. Therefore, the minimum of the µ-CT curve at the pore

356 radius of 10 µm has to be adjusted at $V_c = 1 - 0.639 = 0.361$, because this fraction of pore volume is related

357 to pore body radii smaller than 10 µm.

358 The T_2 relaxation time distribution of sample RÖ10B is plotted in Figure 6. It indicates a distinct maximum

359 at a relaxation time of 170 ms. Non-vanishing signals are observed at relaxation times below 0.1 ms. This is

360 an indication of the existence of very small pores in the Röttbacher sandstone.

361 The position of the NMR curve in the plot of Figure 8 depends on the surface relaxivity ρ. A coincidence

362 with the µ-CT curve at $V_c = 0.5$ requires a surface relaxivity of $\rho = 237$ µm/s for adjusting the NMR curve.

363 The complex conductivity spectra of the Röttbacher sample are displayed in Figure 7. The processing of the

364 spectra according to the described algorithm results in the V_c - r – curve as shown in Figure 8. The SIP

365 curve is fixed at the value $V_c = 0.9$ that has been determined by MIP for the maximum pore radius resolved

366 by SIP ($r_t = 10$ µm).

367 **5 Discussion**

368 Previous studies have compared the V_c - r – curves resulting from different methods (e.g. Zhang and Weller,

369 2014; Zhang et al., 2017; Ding et al., 2017). The slope of the curves was used to get a fractal dimension. It

370 became obvious that the distribution curves indicate remarkable differences that are caused by the physical

371 principles of the used methods. The methods differ with regard to their limits of resolution. The effective

372 resolution of µ-CT is limited by the voxel size. Larger pores can be easily detected. Nevertheless, even

373 though the derived image (voxel) resolution is quite high (1.75 µm), both sandstone data sets feature no

374 significant volume of pore body radii smaller than 10 µm (BH-5) and 17 µm (RÖ-10), respectively. We

375 assume that this is caused by a complex and sensitive mixture of issues about image resolution, image

376 quality (phase contrast), reliability of the watershed-algorithm concerning the separation of individual pores,

377 and hence of the complexity of the pore structure of small pores. The MIP yields the widest range of pore

378 throat radii. The pore radius is directly related to the pressure. A similarly wide range of pore body radii

379 can be resolved by NMR. However, the transformation of the NMR transversal relaxation time into a pore

380 radius requires the surface relaxivity as scaling factor. In a similar way, the transformation of the electrical

381 relaxation time resulting from SIP into a pore radius is based on a scaling factor that depends on the

382 diffusion coefficient. Only a restricted range of pore radii can be resolved by SIP.

383 Beside the range of pore radii, the geometrical extent of the pore radius differs among the methods. µ-CT

384 enables a geometrical description of the individual pore space considering the shape of the pore. The pore

385 radius can be determined in different ways. We use the average pore radius as an equivalent for the pore

386 body radius r_b. MIP is sensitive to the pore throat radius r_t that enables the access to larger pores behind the

387 throat. The NMR relaxation time is related the pore body radius r_b. We assume that the IP signals are

388 caused by the ion-selected active zones in the narrow pores that are comparable with the pore throats.

389 Regarding the differences of the methods, we present an approach that combines the curves to get more

390 information on the pore space. Considering the two kinds of pore radii r_b and r_t, we use first µ-CT and

391 NMR to generate a combined curve displaying V_c as a function of r_b. In the next step, we link the curves

392 resulting from MIP and SIP to get a curve showing V_c as a function of the pore throat radius r_t.

393 It is fundamental that the total pore volume (or total porosity) has to be known. The cumulative pore

394 volume fraction should only consider the pore volume that is resolved in the regarded range of pore radii.

395 Considering the resolution of µ-CT, only the pore space with radii larger than the voxel size is determined.

396 The cumulative pore volume fraction at the limit of resolution has to be adjusted to the non-resolved pore

397 volume. In this way, the µ-CT curve gets a fixed position in the $V_c - r$ plot. Regarding NMR, the relaxation

398 time T_2 has to be transformed into a pore radius according to Eq. (5). The application of Eq. (5) requires the

399 knowledge of the surface relaxivity ρ, which is the necessary scaling factor that causes a shift of the $V_c - r$

400 curve along the axis of pore radius. Since NMR method is sensitive to the pore body radius, we expect a

401 similar $V_c - r$ curve for NMR and µ-CT in the overlapping range of pore body radii. The NMR curve is

402 shifted along the axis of pore body radii until a good agreement between the two curves is reached. This

403 procedure enables the determination of the surface relaxivity. The proposed alternative method for the

404 determination of surface relaxivity considers the reduction of NMR relaxation time T_2 caused by high clay

405 content and iron-bearing minerals (e.g. Keating and Knight, 2010).

406 MIP is used to generate the curve displaying V_c as a function of r_t over a wide range of pore throat radii.

407 The SIP curve is fixed at the MIP curve considering the coincidence at the largest pore radius resolved by

408 SIP.

409 The two curves representing V_c as a function of both r_b and r_t are displayed in a double logarithmic plot.

410 The horizontal shift of the two graphs represents the ratio r_b/r_t. Additionally, the slope of the curves is

411 related to the fractal dimension.

412 The proposed approach in this study results in two pore size distribution curves for the two samples, which

413 are in good accordance to the general pore space structures as described in section 3 and as visualized in

414 Figure 2 (A to F). The first curve combines the distributions resulting from µ-CT and NMR. The µ-CT data

415 provide a pore radius, which is regarded as pore body radius, without any scaling. The scaling of the NMR-

curve provides an estimate of the surface relaxivity. The surface relaxivity of the Bentheimer sample reaches 54 µm/s, the corresponding value of the Röttbacher sample is with 237 µm/s much higher. The higher surface relaxivity in comparison with the Bentheimer sample is clearly justified considering the larger specific surface area (Table 1) and the significantly higher content of clay and iron-bearing minerals as indicated in Table 2.

The two cumulative pore volume distribution curves for the Röttbacher sample (Figure 8) indicate over the wide range of pore radii a parallel progression with consistently higher values for the pore body radius (µ-CT and NMR) in comparison with the pore throat radius (MIP). The horizontal distance of the two curves yields the ratio r_b/r_t. It should be noted that the ratio r_b/r_t may vary with pore sizes. Most studies consider only a fixed ratio r_b/r_t determined from the dominant pore body size from NMR r_b and the dominant pore throat size from MIP r_t (e.g. Müller-Huber et al., 2018). Regarding the median pore radii at $V_c = 0.5$, a ratio $r_b/r_t = 9.13$ is determined. Considering smaller pores, a ratio $r_b/r_t = 12.15$ is indicated at $V_c = 0.05$.

The parallelism of the pore volume distribution curve is less developed for the Bentheimer sample (Figure 4). We observe a clear distance of the two curves in the range of larger pore radii. Regarding the median pore radii at $V_c = 0.5$, a ratio $r_b/r_t = 2.57$ is determined. For $V_c < 0.2$, the slope of the curves decreases and smaller distances between the curves are observed. The NMR curve in Figure 5 indicates for $V_c > 0.08$ larger pore radii in comparison with the MIP curve and confirms the relationship $r_b > r_t$. The reverse behavior in the interval 0.1 µm $< r <$ 0.6 µm is possibly caused by the low volume fraction (3%) attributed to this range of pore radii. It can be expected that the small amount of water in the small pores causes only weak signals in the NMR relaxometry.

Beside the distances between the curves the individual slopes are regarded. The slope (s) of the curve log (V_c) versus log (r) is related to the fractal dimension D of the pore volume ($D = 3 - s$) (Zhang and Weller, 2014). We observe a varying slope in the investigated range of pore radii for the Bentheimer sample. The only range of more or less constant slope, which extends from pore radius 0.1 µm to 10 µm, corresponds to a fractal dimension $D_{MIP} = 2.678$ for MIP, $D_{NMR} = 2.776$ for NMR, and $D_{SIP} = 2.618$ for SIP.

The whole curves of the four methods are non-linear and indicate non-fractal behavior. A Maximum Likelihood Estimator approach (MLE) might be relevant to extract the underlying scaling parameters (Rizzo et al., 2017). For example, in the case of the NMR curve of Bentheimer sandstone, the fitting of all data using the MLE reveals that the log-normal distribution is the most likely distribution with the estimated parameters $\mu = 3.43$ µm and $\sigma = 0.82$ µm. These two scaling parameters are the logarithmic mean and logarithmic standard deviation of the pore radius, respectively. We recognize that the resulting mean radius reaches half value of the effective hydraulic radius ($r_{eff} = 6.97$ µm).

We observe a constant slope of the NMR curve for the Röttbacher sample (Figure 8) in the interval 0.01 µm $< r_b <$ 100 µm. A similar slope is observed for the MIP curve in the interval 0.01 µm $< r_t <$ 10 µm. Considering the overlapping pore throat radii range between 0.1 µm and 10 µm, a fractal dimension D with

451 values of 2.640 for MIP, and 2.661 for NMR has been determined. The slightly higher slope of the SIP

452 curve results in a lower value of fractal dimension of $D = 2.533$.

453 Our approach enables the integration of SIP in the determination of a pore throat size distribution.

454 Considering the limited frequency range, only a limited range of pore throat radii can be reflected. Using a

455 fixed diffusion coefficient $D_{(+)} = 3.8\times10^{-12}$ m²/s, a range of pore throat radii between 0.1 µm and 10 µm is

456 resolved. The SIP curve is linked to the MIP curve at $r = 10$ µm. An extension to lower pore radii would

457 require the integration of higher frequencies. The removal of electromagnetic coupling effects can be one

458 first step to improve the reliability of complex conductivity spectra for frequencies larger than 100 Hz, but

459 it should be regarded that smaller pore sizes are hidden by Maxwell Wagner and dielectric relaxation. The

460 proposed procedure results in a fair agreement between SIP and MIP curves in the overlapping range of

461 pore throat radius for both the Bentheimer and the Röttbacher sample. In comparison with MIP, a slight

462 overestimation of V_c is observed for larger pore throat radii and a underestimation for lower pore throat

463 radii. Considering the two samples of the presented study, the assumption of a constant diffusion

464 coefficient seems to be justified. Though alternative kernels have not been tested, our study confirms that

465 the Debye decomposition provides a relaxation time distribution of complex conductivity spectra that can

466 be transformed in a pore throat size distribution comparable with the resulting curves from MIP. Regarding

467 the discussion on the most relevant parameter that controls the relaxation time, our assumption that the pore

468 throat radius is related to the relaxation time is supported by the results.

469 The investigations by µ-CT, MIP, NMR, and SIP on the sandstone samples have been done in the

470 laboratory. µ-CT and MIP are methods that can only be applied on rock samples. The potential of these

471 methods to derive pore size distributions is well acknowledged. NMR and SIP are methods that can also be

472 performed in boreholes or as field survey. The NMR method has been successfully applied in permeability

473 prediction at the field scale. A variety of permeability prediction models based on SIP parameters has been

474 proposed based on laboratory investigations (e.g. Robinson et al., 2018). First tests have demonstrated their

475 applicability in the field. Most permeability models consider pore size and porosity as the most important

476 parameters. The evaluation of pore sizes of sediments at the field scale is a challenging task for geophysical

477 methods. Our laboratory study has demonstrated the potential of SIP in identifying a pore size distribution.

478 Further investigations with larger sets of samples have to be done to improve the proposed procedure

479 before the pore size distribution can be extracted from high quality complex conductivity field spectra.

480 **6 Conclusions**

481 Pore radii distributions (considering both pore body and pore throat radii) have been determined by

482 different methods (µ-CT, MIP, NMR, and SIP) for two sandstone samples. The curves presenting the

483 cumulative distribution of pore volume V_c as a function of pore size have proved to be a suitable tool for

484   comparison. It becomes obvious that the distribution curves indicate remarkable differences that are based

485   on the physical principles of the used methods. The methods differ with regard to their limits of resolution.

486   The effective resolution of μ-CT is limited by the voxel size (1.75 μm). Larger pores can be easily detected,

487   whereas quantification of small pores and volumes of pores with small radii is severely affected by the

488   image quality and the image processing algorithms. The MIP yields the widest range of pore radii. The pore

489   throat radii are directly related to the pressure interval. A similar wide range of pore radii can be achieved

490   by NMR. However, the transformation of the NMR transversal relaxation time into a pore body radius

491   requires the surface relaxivity as scaling factor. In a similar way, the transformation of the electrical

492   relaxation time resulting from SIP into a pore radius is based on a scaling factor that depends on the

493   diffusion coefficient. Only a restricted range of pore radii (0.1 μm to 10 μm) can be resolved by SIP.

494   Beside the range of pore radii, the geometrical extent of the pore radius differs among the methods. μ-CT

495   enables a geometrical description of the individual pore space considering the shape of the pore. The pore

496   radius can be determined in different ways. We use the average pore radius as an equivalent for the pore

497   body radius r_b. MIP is sensitive to the pore throat radius r_t that enables the access to larger pores behind the

498   throat. The NMR relaxation time is related to an average pore body radius r_b. We assume that the IP signals

499   are caused by the ion-selected active zones in the narrow pores that are comparable with the pore throats.

500   Considering the two kinds of pore radii r_b and r_t, we use μ-CT and NMR to generate a combined curve

501   displaying V_c as a function of r_b. A good agreement between the two curves is achieved if they coincide at

502    $V_c = 0.5$. This condition is used to determine the surface relaxivity, which is in good accordance to the

503   investigated surface area and mineralogy of the sample materials. MIP is used to generate the curve

504   displaying V_c as a function of r_t over a wide range of pore throat radii. The SIP curve is fixed at the MIP

505   curve considering the coincidence at the largest pore radius resulting from SIP.

506   The two curves representing V_c as a function of both r_b and r_t are displayed in a double logarithmic plot.

507   The horizontal shift of the two graphs represents the ratio r_b/r_t. Additionally, the slope of the curves is

508   related to the fractal dimension.

509   The investigations on the samples demonstrate that the porosity increases using a method with a higher

510   resolution. Both porosity and pore volume are parameters that depend on the resolution. The fractal

511   dimension describes the size of geometric objects as a function of resolution. Therefore, the knowledge of

512   fractal behavior enables upscaling and downscaling of geometric quantities. The Bentheimer sandstone

513   sample is characterized by a ratio $r_b/r_t = 2.57$ for the larger pores. A fractal behavior is observed in the

514   range of pore radii between 0.1 μm and 10 μm with an average $D = 2.69$ determined for the pore volume by

515   MIP, NMR, and SIP. The Röttbacher sandstone sample indicates with $r_b/r_t = 9.13$ a larger ratio between

516   pore body radius and pore throat in comparison with the Bentheimer sample. An average fractal dimension

517   of $D = 2.61$ is determined for the Röttbacher sample.

518   **Acknowledgements**

519   The authors thank Sven Nordsiek (University Bayreuth) for the Debye decomposition of the SIP data,

520   Dietmar Meinel (BAM, Berlin) for supporting the CT analysis, Carsten Prinz (BAM, Berlin) for providing

521   the MIP data, and Mike Müller-Petke as well as Raphael Dlugosch (both Leibniz Institute for Applied

522   Geophysics, Hanover) for the acquisition of the NMR spectra for this study. Dr. Zeyu Zhang thanks

523   Bundesanstalt für Materialforschung und –prüfung (BAM, Berlin) for the Adolf-Martens-Fellowship that

524   enabled his stay in Germany for the experimental research.

525   **References**

526   API (American Petroleum Institute): Recommended Practices for Core Analysis. API Recommended

527   Practice 40, chapter 6 – permeability determination, second edition, February 1998.

528   Avnir, D., and Jaroniec, M.: An isotherm equation for adsorption on fractal surfaces of heterogeneous

529   porous materials, Langmuir, 5, 6, 1412–1433, 1989.

530   Avnir, D., Farin, D., and Pfeifer, P.: Molecular fractal surfaces, Nature, 308, 261-263, 1984.

531   Behroozmand, A., Keating, K., and Auken, E.: A review of the principles and applications of the NMR

532   technique for near-surface characterization, Surv Geophys, 36, 27–85, doi: 10.1007/s10712-014-9304-0,

533   2015.

534   Binley, A., Slater, L. D., Fukees, M., and Cassiani, G.: Relationship between spectral induced polarization

535   and hydraulic poroperties of saturated and unsaturated sandstone, Water Resources Research, 41, W12417,

536   doi:10.1029/2005WR004202 , 2005.

537   Ding, Y., Weller, A., Zhang, Z., and Kassab, M.: Fractal dimension of pore space in carbonate samples

538   from Tushka Area (Egypt), Arabian Journal of Geosciences, 10, 388, doi: 10.1007/s12517-017-3173-z,

539   2017.

540   Dubelaar, W. C., and Nijland, T. G.: The Bentheim Sandstone: geology, petrophysics, varieties and its use

541   as dimension stone, in: Engineering Geology for Society and Territory, 8, Lollino, G., Giordan, D.,

542   Marunteanu, C., Christaras, B., Yoshinori, I., and Margottini, C. (Eds.), Springer International Publishing,

543   Switzerland, 557-563, 2015.

544   Florsch, N., Revil, A., and Camerlynck, C.: Inversion of generalized relaxation time distributions with

545   optimized samping parameter, Journal of Applied Geophysics, 109, 119-132, 2014.

546   Gaboreau, S., Robinet, J. C., Tournassat, C., and Savoye, S.: Diffuse transport in clay media: µm to nm
547   scale characterization of pore space and mineral spatial organization: International Meeting Clays in
548   Natural and Engineered Barriers for Radioactive Waste Confinement, Montpellier, France, October 2012,
549   hal-00705345, 2012.

550   Halisch, M., Schmitt, M., and Fernandes, C. P.: Pore Shapes and Pore Geometry of Reservoirs Rocks from
551   µ-CT Imaging and Digital Image Analysis, in: Proceedings of the Annual Symposium of the SCA 2016,
552   Snowmass, Colorado, USA, 21-26 August 2016, SCA2016-093, 2016.

553   Halisch, M., Steeb, H., Henkel, S., and Krawczyk, C. M.: Pore-Scale tomography and imaging:
554   applications, techniques and recommended practice, Solid Earth Special Issue, Solid Earth, 7, 1141-1143,
555   doi:10.5194/se-7-1-2016, 2016.

556   Keating, K., and Knight, R.: A laboratory study of the effect of Fe(II)-bearing minerals on nuclear magnetic
557   resonance (NMR) relaxation measurements, Geophysics, 75, 3, F71–F82, 2010.

558   Keller, L. M., Holzer, L., Wepf, R., Gasser, P., Münch, B., and Marschall, P.: On the application of focused
559   ion beam nanotomography in characterizing the 3D pore space geometry of Opalinus clay, Physics and
560   Chemistry of the Earth, 36, 1539-1544, doi:10.1016/j.pce.2011.07.010, 2011.

561   Kelokaski, M., Siitari-Kauppi, M., Sardini, P., Mori, A., and Hellmuth, K.H.: Characterisation of pore
562   space geometry by ^{14}C-PMMA impregnation-development work for in situ studies, Journal of Geochemical
563   Exploration,   90, 45-52, doi:10.1016/j.gexplo.2005.09.005, 2005.

564   Kleinberg, R. L.: Utility of NMR T_2 distributions, connection with capillary pressure, clay effect, and
565   determination of the surface relaxivity parameter ρ2, Magnetic Resonance Imaging, 14, 761–767, 1996.

566   Klinkenberg, L. J.: The permeability of porous media to liquids and gases, API Drill and Production
567   Practices, 200-213, 1941.

568   Kruschwitz, S., Prinz C., and Zimathies A.: Study into the correlation of dominant pore throat size and SIP
569   relaxation frequency, Journal of Applied Geophysics, 135, 375-386, 2016.

570   Leroy, P., Revil, A., Kemna, A., Cosenza, P., and Gorbani, A.: Spectral induced polarization of water-
571   saturated packs of glass beads, J. Colloid Interface Sci, 321, 103-117, doi:10.1016/j.jcis.2007.12.031, 2008.

572   Mandelbrot, B. B.: Fractals: form, chance, and dimension, Freeman, San Francisco, 1977.

573   Mandelbrot, B. B.: Fractal geometry of nature, Freeman, San Francisco, 1983.

574 Mancuso, C., Jommi, C., and D'Onza, F. (Eds.): Unsaturated Soils: Research and Applications, Volume 1,

575 Springer-Verlag Berlin Heidelberg, 123-130, doi: 10.1007/978-3-642-31116-1, ISBN: 978-3-642-31115-4

576 (Print), 2012.

577 Mees, F., Swennen, R., van Geet, M., and Jacobs, P. (Eds.): Applications of X-ray computed tomography

578 in the geosciences, Geological Society, London, Special Publication, 215, 1, 1-6, doi:

579 10.1144/GSL.SP.2003.215.01.01, 2003.

580 Meyer, K., Klobes, P., and Röhl-Kuhn, B.: Certification of reference material with special emphasis on

581 porous solids, Crystal Research and Technol., 32, 173-183, 1997.

582 Müller-Huber, E., Börner, F., Börner, J. H., and Kulke, D.: Combined interpretation of NMR, MICP, and

583 SIP measurements on mud-dominated and grain-dominated carbonate rocks, Journal of Applied

584 Geophysics, 159, 228–240, doi: 10.1016/j.jappgeo.2018.08.011, 2018.

585 Niu, Q., and Revil, A.: Connecting complex conductivity spectra to mercury porosimetry of sedimentary

586 rocks, Geophysics, 81, E17-E32, doi:10.1190/GEO2015-0072.1, 2016.

587 Niu, Q., and Zhang, C.: Joint inversion of NMR and SIP data to estimate pore size distribution of

588 geomaterials, Geophysical Journal International, 212 (3), 1791-1805, doi: 10.1093/gji/ggx501, 2017.

589 Nordsiek, S., and Weller, A.: A new approach to fitting induced-polarization spectra, Geophysics, 73, 6,

590 F235-F245, doi: 10.1190/1.2987412, 2008.

591 Pape, H., Riepe, L., and Schopper, J. R.: A pigeon-hole model for relating permeability to specific surface,

592 The Log Analyst, 23, 1, 5–13, 1982.

593 Pape, H., Arnold J., Pechnig R., Clauser C., Talnishnikh E., Anferova S., and Blümlich B.: Permeability

594 prediction for low porosity rocks by mobile NMR, Pure and Applied Geophysics, 166, 1125-1163, 2009.

595 Peksa, A., Wolf, K., and Zitha, P.: Bentheimer sandstone revisited for experimental purposes, Marine and

596 Petroleum Geology, 67, 701-719, doi: 10.1016/j.marpetgeo.2015.06.001, 2015.

597 Peth, S., Horn, R., Beckmann, F., Donath, T., Fischer, J., and Smucker, A. J. M.: Three-dimensional

598 quantifi cation of intra-aggregate pore-space features using Synchrotron-Radiation-Based

599 Microtomography, Soil Science Society of America journal, 72, 4, 897-907, doi: 10.2136/sssaj2007.0130,

600 2008.

601 Revil, A., and Florsch, N.: Determination of permeability from spectral induced polarization data in
602 granular media, Geophysical Journal International, 181, 1480-1498, 2010.

603 Revil, A., Koch, K., and Holliger, K.: Is it the grain size or the characteristic pore size that controls the
604 induced polarization relaxation time of clean sands and sandstones?, Water Resources Research, 48,
605 W05602, doi: 10.1029/2011WR011561, 2012.

606 Revil, A.: Effective conductivity and permittivity of unsaturated porous materials in the frequency range 1
607 mHz-1GHz, Water Resources Research, 49, 306-327, doi: 10.1029/2012WR012700, 2013.

608 Revil, A., Florsch, N., and Camerlynck, C.: Spectral induced polarization porosimetry, Geophysical Journal
609 International, 198, 1016-1033, doi: 10.1093/gji/ggu180, 2014.

610 Rieckmann, M.: Untersuchung von Turbulenzerscheinungen beim Fließen von Gasen durch
611 Speichergesteine unter Berücksichtigung der Gleitströmung, Erdöl-Erdgas-Zeitschrift, 6, 36-51, 1970.

612 Rizzo, R.E., Healy, D., and De Siena, L.: Benefits of maximum likelihood estimators for fracture attribute
613 analysis: Implications for permeability and up-scaling, Journal of Structural Geology, 95, 17-31, doi:
614 10.1016/j.jsg.2016.12.005, 2017.

615 Robinson, J., Slater, L., Weller, A., Keating, K., Robinson, T., Rose, C., and Parker, B.: On permeability
616 prediction from complex conductivity measurements using polarization magnitude and relaxation time,
617 Water Resources Research, 54, https://doi.org/10.1002/2017WR022034, 2018.

618 Rouquerol, J., Avnir, D., Fairbridge, D. C. W., Everett, D. H., Haynes, J. H., Pernicone, N., Ramsay, J. D.
619 F., Sing, K. S. W., and Unger, K. K.: Recommendations for the characterization of porous solids (Technical
620 Report), Pure and Appl. Chem., 66, 1739-1758, 1994.

621 Schleifer, N., Weller, A., Schneider, S., and Junge, A.: Investigation of a Bronze Age plankway by spectral
622 induced polarization, Archeological Prospection, 9, 243–253, doi: 10.1002/arp.194, 2002.

623 Schmitt, M., Halisch, M., Müller, C., and Fernandes, C. P.: Classification and quantification of pore shapes
624 in sandstone reservoir rocks with 3-D X-ray micro-computed tomography, Solid Earth, 7, 285–300,
625 doi:10.5194/se-7-285-2016, 2016.

626 Schwarz, G.: A theory of the low-frequency dielectric dispersion of colloidal particles in electrolyte
627 solution, Journal of Physical Chemistry, 66, 2636-2642, doi: 10.1021/j100818a067, 1962.

628 Scott, J. B. T., and Barker, R. D.: Determining pore-throat size in Permo-Triassic sandstones from low-
629 frequency electrical spectroscopy, Geophysical Research Letters, 30, 1450, doi: 10.1029/2003GL016951,
630 2003.

631 Silin, D. and Patzek, T.: Pore space morphology analysis using maximal inscribed spheres, Physica A, 371,
632 2,336-360, doi: 10.1016/j.physa.2006.04.048, 2006.

633 Slater, L., and Lesmes, D. P.: Electric-hydraulic relationships observed for unconsolidated sediments,
634 Water Resources Research, 38, 10, doi:10.1029/2001WR001075, 2002.

635 Terasov, A., and Titov, K.: Relaxation time distribution from time domain induced polarization
636 measurements, Geophysical Journal International, 170, 31-43, doi: 10.1111/j.1365-246X.2007.03376.x,
637 2007.

638 Thomeer, J. H. M.: Introduction of a pore geometrical factor defined by the capillary pressure curve,
639 Journal of Petroleum Technology, 12(3), 73-77, 1960.

640 Washburn, E. W.: The dynamics of capillary flow, Physical Review, 17, 3, 273-283, 1921.

641 Weigand, M., and Kemna, A.: Debye decomposition of time-lapse spectral induced polarization data,
642 Computers & Geosciences, 86, 34-45, http://dx.doi.org/10.1016/j.cageo.2015.09.021, 2016.

643 Weller, A., Zhang, Z., Slater, L., Kruschwitz, S., and Halisch, M.: Induced polarization and pore radius – a
644 discussion, Geophysics, 81, 5, D519-526, doi:10.1190/GEO2016-0135.1, 2016.

645 Weller, A., Slater, L., Binley, A., Nordsiek, S., and Xu, S.: Permeability prediction based on induced
646 polarization: Insights from measurements on sandstone and unconsolidated samples spanning a wide
647 permeability range, Geophysics, 80, 2, D161-D173, doi:10.1190/GEO2014-0368.1, 2015.

648 Weller, A., Nordsiek, S., and Debschütz, W.: Estimating permeability of sandstone samples by nuclear
649 magnetic resonance and spectral-induced polarization, Geophysics, 75, E215 – E226, doi:
650 10.1190/1.3507304, 2010.

651 Zhang, Z., Weller, A., and Kruschwitz, S.: Pore radius distribution and fractal dimension derived from
652 spectral induced polarization, Near Surface Geophysics, 15, 625-632, doi: 10.3997/1873-0604.2017035,
653 2017.

654 Zhang, Z., and Weller, A.: Fractal dimension of pore space geometry of an Eocene sandstone formation,
655 Geophysics, 79, D377-387, doi:10.1190/GEO2014-0143.1, 2014.

656 Zimmermann, E., Kemna, A., Berwix, J., Glaas, W., and Vereecken., H.: EIT measurement system with

657 high phase accuracy for the imaging of spectral induced polarization properties of soils and sediments,

658 Measurement Science and Technology, 19, 9, 094010, doi: 10.1088/0957-0233/19/9/094010, 2008.

659

660 **Table 1: Petrophysical properties of the samples: porosity ϕ, permeability K, specific surface area S_m, formation**
661 **factor F, dominant pore radius r_{dom}, effective pore radius r_{eff}, the ratio r_b / r_t, fractal dimensions determined from**
662 **mercury intrusion porosimetry D_{MIP}, nuclear magnetic resonance D_{NMR}, and spectral induced polarization D_{SIP},**
663 **the surface relaxivity ρ, and the Diffusion coefficient $D_{(+)}$.**
664

	unit	BH5-2	RÖ10B
Porosity (triple weighing)		0.238	0.159
Porosity (μ-CT)		0.184	0.106
Porosity (MIP)		0.238	0.166
Permeability K	m²	4.25×10^{-13}	3.45×10^{-14}
Specific surface area	m²/g	0.30	1.98
Formation factor F		14.3	11.3
r_{dom} (MIP)	μm	11.4	4.9
$r_{eff} = (8FK)^{0.5}$	μm	6.97	1.77
r_b / r_t		2.57	9.13
D_{MIP}		2.678	2.640
D_{NMR}		2.776	2.661
D_{SIP}		2.618	2.533
Surface relaxivity ρ	μm/s	54	237
Diffusion coefficient $D_{(+)}$	m²/s	3.8×10^{-12}	3.8×10^{-12}

665
666 **Table 2: Chemical components of the samples from X-ray Fluorescence analysis.**
667

	Selected chemical components from X-Ray Fluorescence [weight-%]						
Sample	SiO_2	TiO_2	Al_2O_3	Fe_2O_3	CaO	Na_2O	K_2O
BH5-2	97.84	0.048	1.2	0.05	0.019	0.02	0.355
RÖ10B	87.06	0.356	6.06	1.07	0.225	0.13	3 679

668
669

670   **Table 3: Geometrical parameters of individual pores derived from µ-CT data of the two samples.**

descriptor	Sample					
	BH5-2			RÖ10B		
	min. [µm]	max. [µm]	mean [µm]	min. [µm]	max. [µm]	mean[µm]
equivalent pore diameter	2.17	229.1	71.56	1.86	230.4	28.95
Feret length (length 3D)	1.92	537.1	161.8	1.64	416.8	56.3
Feret Width (width 3D)	1.92	307.0	87.45	1.64	265.8	28.28
Feret breadth (breadth 3D)	1.75	379.4	114.7	1.5	354.8	37.99
pore volume [µm³]	5.36	6294270	315069	3.38	6404830	64809

671
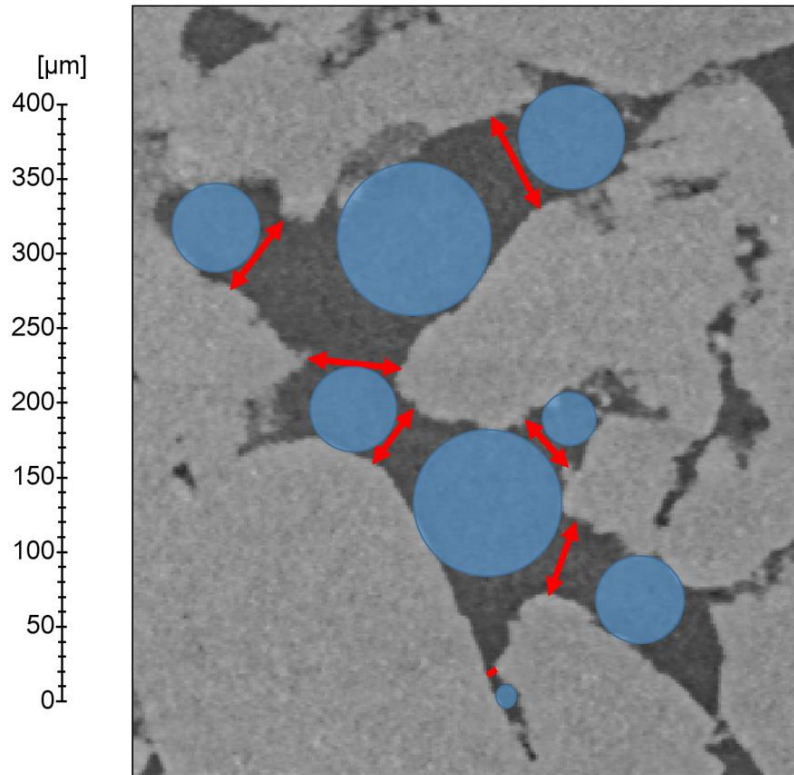
Figure 1: Zoomed in 2-D slice view of sample BH-5 in order to visualize pore bodies (blue circles, detected by NMR and DIA of µ-CT data) and pore throats (red lines with arrows, detected by MIP).
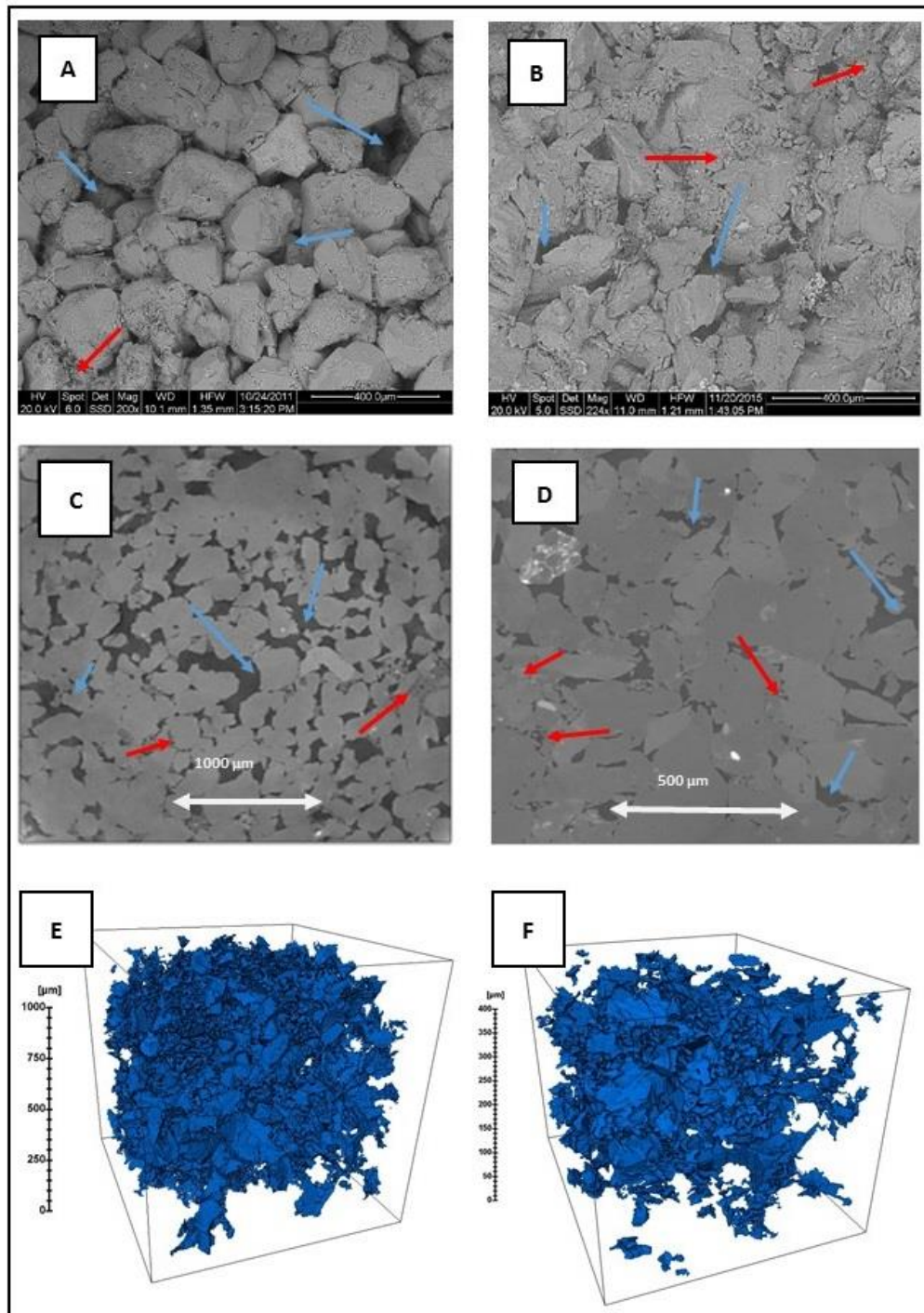
677
678
679 Figure 2: SEM (A) and 2D (C) and 3D (E) CT views upon the minerals and pore structure of the investigated
680 sample of Bentheimer sandstone, and SEM (B) and 2D (D) and 3D (F) CT views upon the minerals and pore
681 structure of the investigated sample of Röttbacher sandstone. Blue arrows indicate open pore spaces, red arrows
682 indicate clay agglomerations and pore fillings.
683
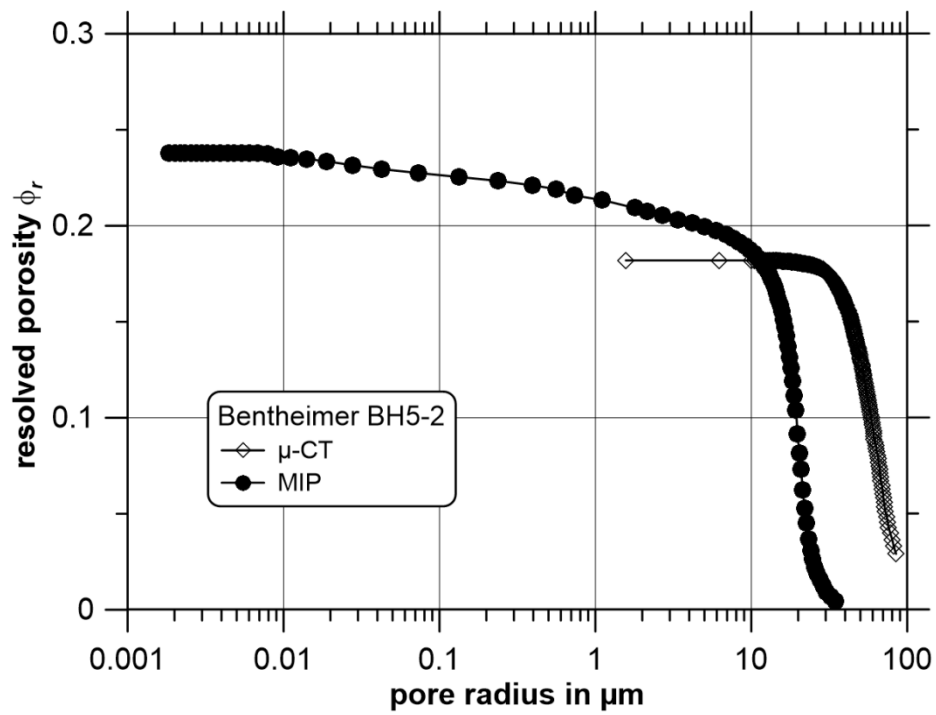
684
685
686 **Figure 3: The recognized porosity and pore size range of Bentheimer sandstone sample BH5-2. The maximum**
687 **porosity recognized by MIP is 0.238 and the maximum porosity recognized by μ-CT is 0.184.**
688
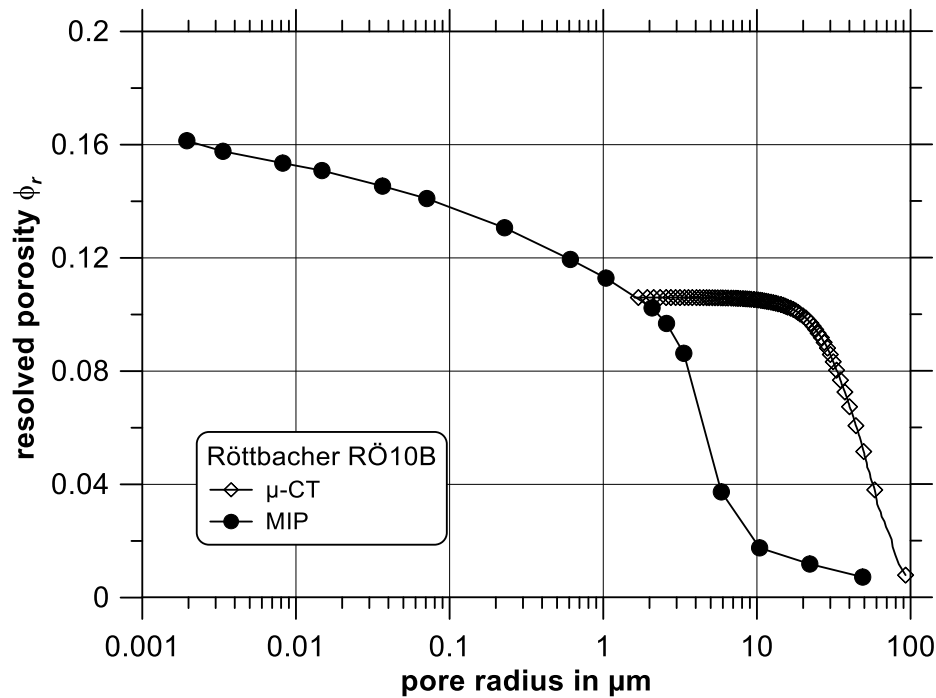
689
690
691 **Figure 4: The recognized porosity and pore size range of Röttbacher sandstone sample RÖ10B. The maximum**
692 **porosity recognized by MIP is 0.166 and the maximum porosity recognized by μ-CT is 0.106.**
693
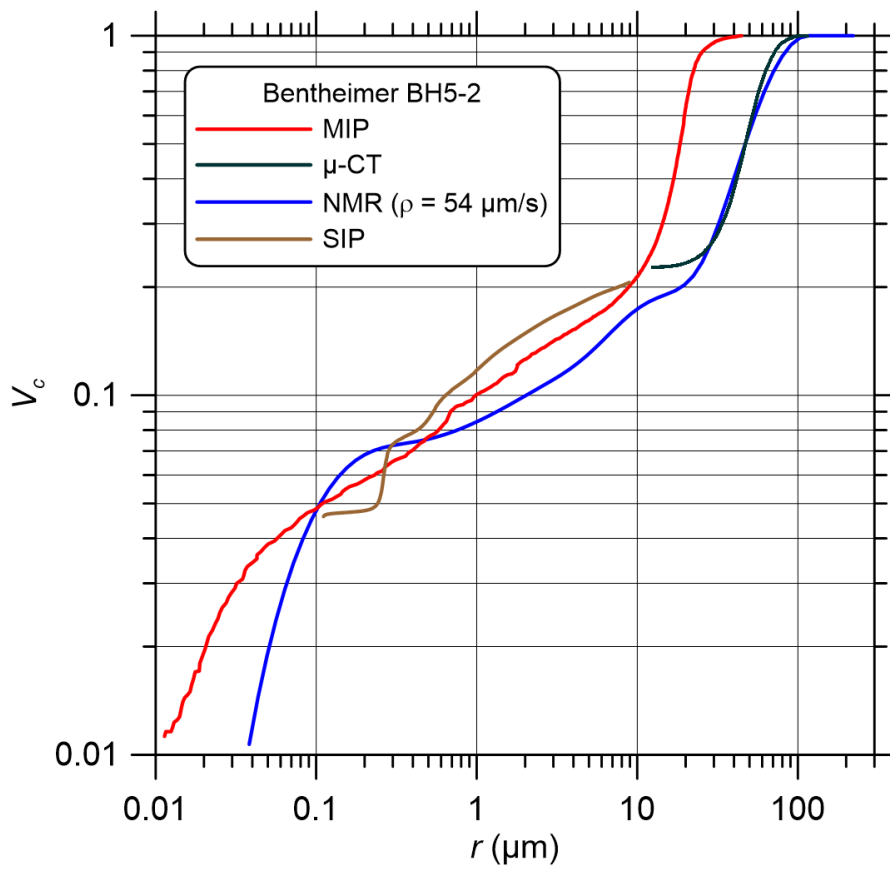
694
695
696 **Figure 5: The comparison of V_c-r curves determined from MIP, μ-CT, NMR and SIP for Bentheimer sandstone**
697 **sample BH5-2.**
698
699
700
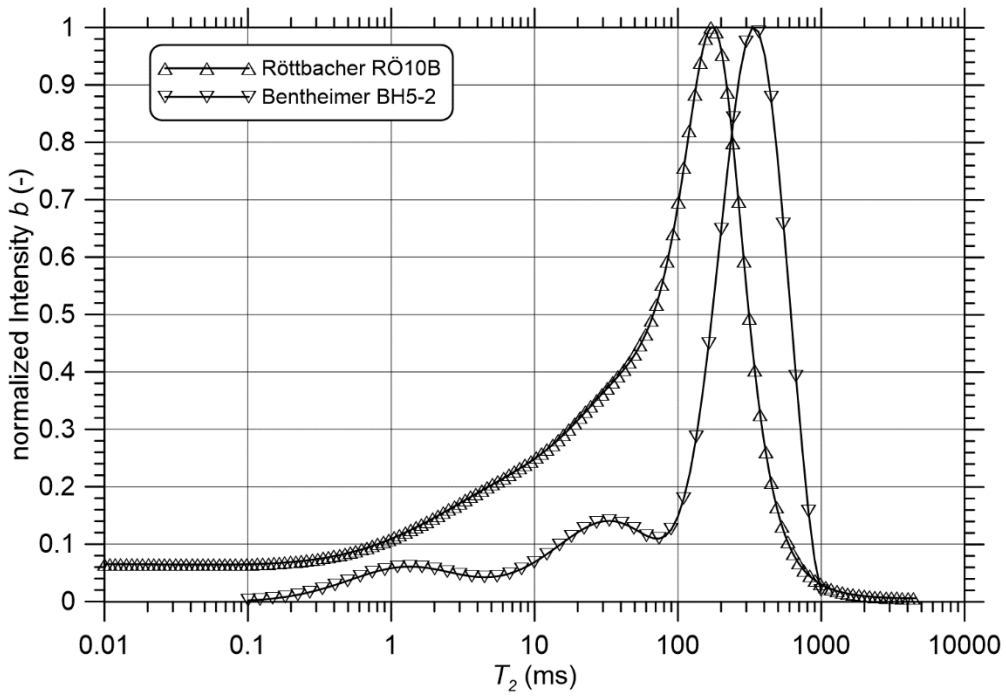
701
702
703 **Figure 6: The NMR T_2 relaxation time distributions of samples BH5-2 and RÖ10B.**
704

705
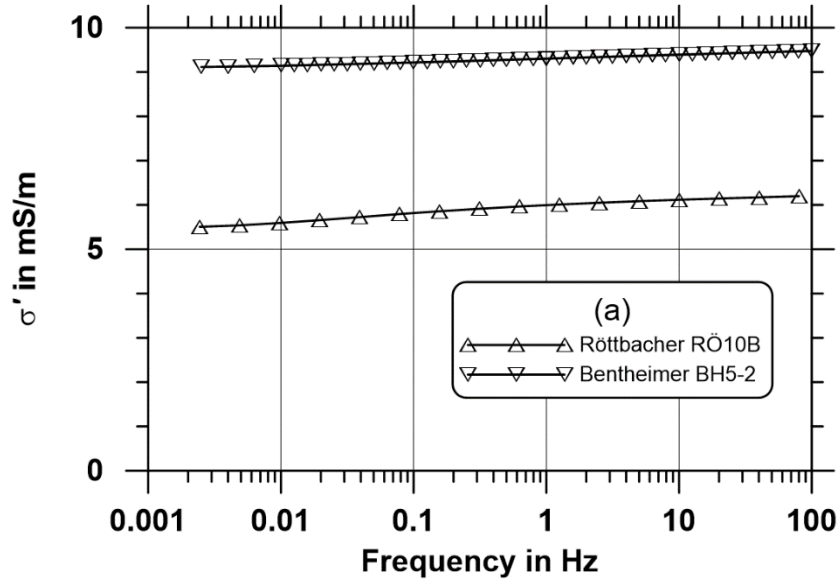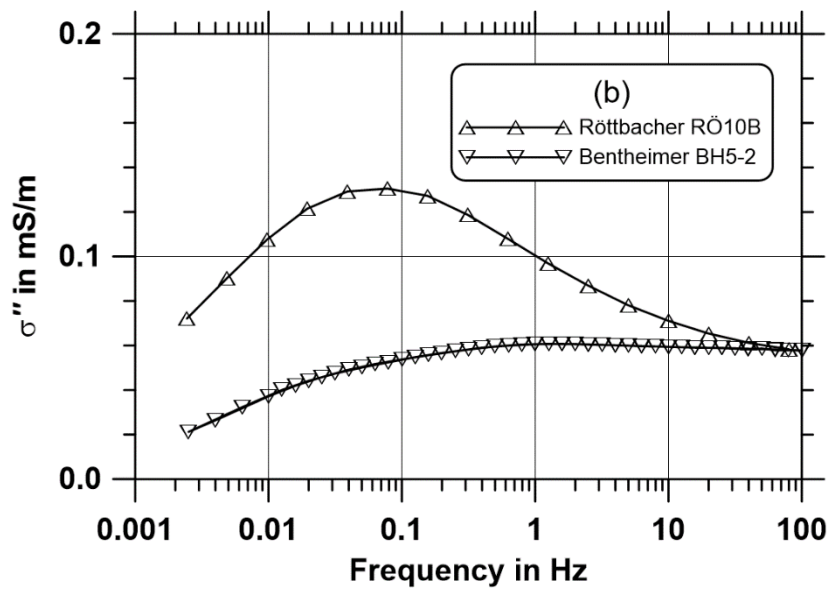
Figure 7: Measured complex conductivity spectra of samples BH5-2 and RÖ10B. a) real part of conductivity, b) imaginary part of conductivity.
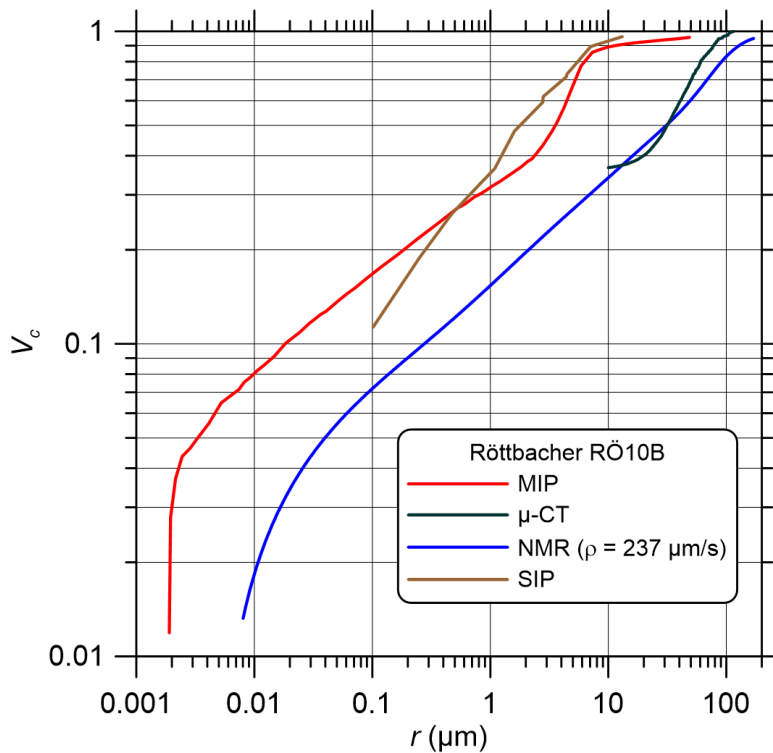
Figure 8: The comparison of V_c-r curves determined from MIP, μ-CT, NMR and SIP for Röttbacher sandstone sample RÖ10B.